

Highly Morphology-Controllable and Highly Sensitive Capacitive Tactile Sensor Based on Epidermis-Dermis-Inspired Interlocked Asymmetric-Nanocone Arrays for Detection of Tiny Pressure

Hongsen Niu, Song Gao, Wenjing Yue, Yang Li,* Weijia Zhou,* and Hong Liu*

The tactile sensor lies at the heart of electronic skin and is of great importance in the development of flexible electronic devices. To date, it still remains a critical challenge to develop a large-scale capacitive tactile sensor with high sensitivity and controllable morphology in an economical way. Inspired by the interlocked microridges between the epidermis and dermis, herein, a highly sensitive capacitive tactile sensor by creating interlocked asymmetric-nanocones in poly(vinylidene fluoride-co-trifluoroethylene) film is proposed. Particularly, a facile method based on cone-shaped nanoporous anodized aluminum oxide templates is proposed to cost-effectively fabricate the highly ordered nanocones in a controllable manner and on a large scale. Finite-element analysis reveals that under vertical forces, the strain/stress can be highly strengthened and localized at the contact apexes, resulting in an amplified variation of film permittivity and thickness. Benefiting from this, the developed tactile sensor presents several conspicuous features, including the maximum sensitivity (6.583 kPa^{-1}) in the low pressure region (0–100 Pa), ultralow detection limit ($\approx 3 \text{ Pa}$), rapid response/recovery time (48/36 ms), excellent stability and reproducibility (10 000 cycles). These salient merits enable the sensor to be successfully applied in a variety of applications including sign language gesture detection, spatial pressure mapping, Braille recognition, and physiological signal monitoring.

1. Introduction


As the largest sensory organ in human body, skin can perceive and interpret various external stimuli such as vibration, pressure, and strain via its tactile sensory system which is mainly composed of several sensory neurons. For instance, Ruffini ending can respond to the stretching and deformation of skin, while Meissner corpuscle enables the feeling of movement and fluttering touch on human skin. In addition, the sensation of texture, curvature, and shape of an object can be realized by Merkel cell.^[1,2] Recently, to mimic the sensing mechanism of human skin, researchers have developed highly sensitive and flexible electronic skin (e-skin) by converting external stimuli including strain, pressure, and distortion to recordable or measurable electronic signals (i.e., current, voltage, resistance, and capacitance). In light of its practical usage in prominent applications encompassing wearable devices,^[3,4] personal healthcare,^[5–7] and human motion monitoring,^[8–10] the e-skin has attracted drastically growing interest.

A flexible tactile sensor is the core part of the e-skin and is mainly used to imitate the tissue structure between dermis and epidermis of the human skin. Depending on the mechanism of sensing, it can be generally categorized into four representative types: capacitive tactile sensor,^[11–13] piezoelectric tactile sensor,^[14–16] piezoresistive tactile sensor,^[17–19] and triboelectric tactile sensor.^[20–22] In particular, capacitive tactile sensor has received burgeoning amount of interest in recent years considering its superior merits including low power consumption, simple governing equation, low detection limit, fast response time, and high stability. The capacitive tactile sensor typically resorts to a “sandwich” configuration consisting of two electrode layers at the top and bottom and one dielectric layer in the middle, and the material and structure of dielectric layer are emphatically studied. Thus far, poly(methyl methacrylate) (PMMA) and polydimethylsiloxane (PDMS) are the two most commonly used materials for the dielectric layer. As the PMMA features a high Young’s modulus ($\approx 3 \text{ GPa}$),^[23] its rigidity is

H. Niu, Dr. S. Gao, Dr. W. Yue, Prof. Y. Li
 School of Information Science and Engineering
 University of Jinan
 Jinan 250022, China
 E-mail: ise_liy@ujn.edu.cn

Prof. W. Zhou, Prof. H. Liu
 Institute for Advanced Interdisciplinary Research
 University of Jinan
 Jinan 250022, China
 E-mail: ifc_zhouwj@ujn.edu.cn; hongliu@sdu.edu.cn

Prof. H. Liu
 State Key Laboratory of Crystal Materials
 Shandong University
 Jinan 250100, China

 The ORCID identification number(s) for the author(s) of this article can be found under <https://doi.org/10.1002/smll.201904774>.

DOI: 10.1002/smll.201904774

large and it is difficult to deform under tiny pressure, which will lead to low sensitivity of the sensor. More importantly, it also affects the flexibility of the sensor, which is limited in the application of wearable devices.^[24] While the sensitivity might be enhanced by employing PDMS that exhibits a lower Young's modulus ($\approx 1.74\text{--}2.6$ MPa),^[25] the response and recovery time of the relevant device are likely to be prolonged considering the high viscoelasticity of PDMS.^[26–28] On the other hand, the low dielectric constant values of PMMA (≈ 3.0)^[29] and PDMS (≈ 2.8)^[30] also make them inappropriate for constructing highly integrated capacitive tactile sensors. Generally speaking, a vertical pressure exerting on the capacitive tactile sensor will change the thickness of the dielectric layer and subsequently result in a variation of the capacitance value. Owing to the relatively limited variation range in thickness of the dielectric layer, the sensitivity of such sensor is typically maintained at quite low-level. The utilization of easy-compressed monolayer microstructures such as micropyramids,^[7,31] microdomes,^[32] micropillars,^[33] and micropore^[34,35] in the dielectric layer, has been found to be beneficial in improving the sensitivity of the sensor. While researchers are trying to understand why human skin can respond to external stimuli with a high sensitivity, they discovered the interlocked microstructures locating at the interface between the dermis and epidermis of human skin (Figure 1a). Such structures are able to produce high stress concentration at the tip of the microridges near the sensory neuron, playing a crucial role in ameliorating the afferent stimuli in pressure perception. Inspired by this phenomenon, researchers have exploited interlocked microstructures to develop a colossal amount of high-performance piezoresistive tactile sensors.^[36–42] For example, Ko and co-workers have demonstrated a stretchable piezoresistive tactile sensor incorporating interlocked microdomes made by CNT/PDMS composites and have verified that the interlocked microdomes help to enable higher sensitive detection ability to various mechanical stimuli than the monolayer microdome.^[39] Furthermore, multilayer interlocked microdomes have been recently employed for the construction of a flexible piezoresistive tactile sensor which is able to provide ultrahigh pressure sensitivity and linear response over an extremely broad pressure range.^[40] In these studies, as the stress is highly concentrated at the contact point or the local deformation of the interlocked microdomes, the external stimuli can be more efficiently transformed into electrical signals, resulting in an enhanced sensitivity of the piezoresistive tactile sensor. Nevertheless, due to the high consumption of the DC current, these piezoresistive tactile sensors comprising of interlocked microstructures tend to be a barrier used in wearable devices.

It should be noted that there are two common approaches for manufacturing the aforementioned microstructures. The first approach relies on traditional photolithography technique to prepare a patterned silicon template with conventional microstructures such as micropyramids^[31] and micropillars.^[33] The patterned template then will be transferred to a flexible polymer material so that a uniformly distributed microstructure array can be attained. Despite of its advantage in fabricating microstructures with high accuracy and in a controllable manner, the manufacturing process of such technique is undesirably complicated, time-consuming, and uneconomical. Besides, when the expected patterns reach nanoscale, it is very difficult to precisely control the morphology based on general lithography machine. The second approach exploits natural existing biomaterials such as the mimosa leaves,^[42] *Calathea zebrina* leaves,^[43] banana leaves,^[44] and lotus leaves^[38,45,46] as the templates to directly manufacture the microstructure arrays. This approach is simple, cost-effective and can be used for large-scale fabrication, however, it suffers from a critical demerit that the details of the microstructures such as the shape, dimension, and spacing cannot be arbitrarily controlled as they are primarily related to the natural biomaterial. In general, a highly integrated tactile sensor that can feature both high sensitivity and low power consumption and can be cost-effectively fabricated on large scales, is desperately awaited.

In this work, a facile method based on simple melt infiltration process and commercial cone-shaped nanoporous anodized aluminum oxide (AAO) transfer method is innovatively proposed to fabricate a capacitive tactile sensor with interlocked asymmetric-nanocones (Figure 1b), opening a new avenue for cost-effectively and commercially manufacturing nanoscale microstructures on large scales and in a controllable manner. More importantly, the unpolarized adoption of poly(vinylidene fluoride-co-trifluoroethylene) [P(VDF-TrFE)] which exhibits a low viscoelasticity, medium Young's modulus (≈ 0.86 GPa) and high dielectric constant (about 8–10) as the structural material of the interlocked nanocones,^[47] makes it suitable for constructing miniaturized and highly integrated capacitive tactile sensors. Benefiting from the anticollapse stability of the uniformly and densely distributed nanocones, the proposed tactile sensor holds several merits that it can provide high sensitivity in the low pressure, ultralow detection limit, fast response/recovery time, and superior stability in repeated loading and bending tests. The sensing mechanism has been further examined by carrying out finite-element analysis (FEA) on the interlocked nanocones in this work. Ultimately, the developed tactile sensor/sensor array show excellent

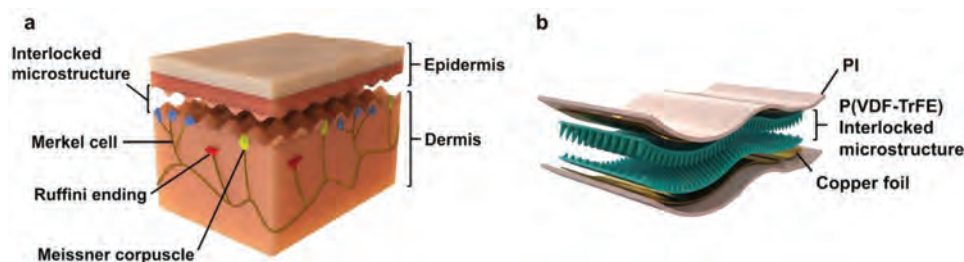


Figure 1. Epidermis-dermis-inspired capacitive tactile sensor. a) Schematic of human skin structure showing interlocked epidermal-dermal layers and several sensory neurons. b) Schematic of the proposed capacitive tactile sensor based on P(VDF-TrFE) films with the interlocked asymmetric-nanocones.

performances in the detection of vertically applied mechanical force, the applications in human-machine interaction and recognition of physiological signals.

2. Results and Discussion

2.1. Preparation and Characterization

Figure 2a illustrates the flow chart of the fabrication procedure for the interlocked nanocones and a schematic of the

ultimately assembled capacitive tactile sensor. Unlike previous works whose dielectric layer is made of PMMA or PDMS and is structured by conventional photolithography technique or biomaterial template, we intentionally use P(VDF-TrFE) polymer as the structural material considering its excellent flexibility and biocompatibility and exploit cone-shaped nanoporous AAO templates (Figure 2a-I) for manufacturing the interlocked nanocones. First, the P(VDF-TrFE)/ *N,N*-dimethylformamide (DMF) solution is spin-coated on top of two cone-shaped nanoporous AAO templates with distinct hole depth of 900 and 400 nm to initialize the fabrication procedure

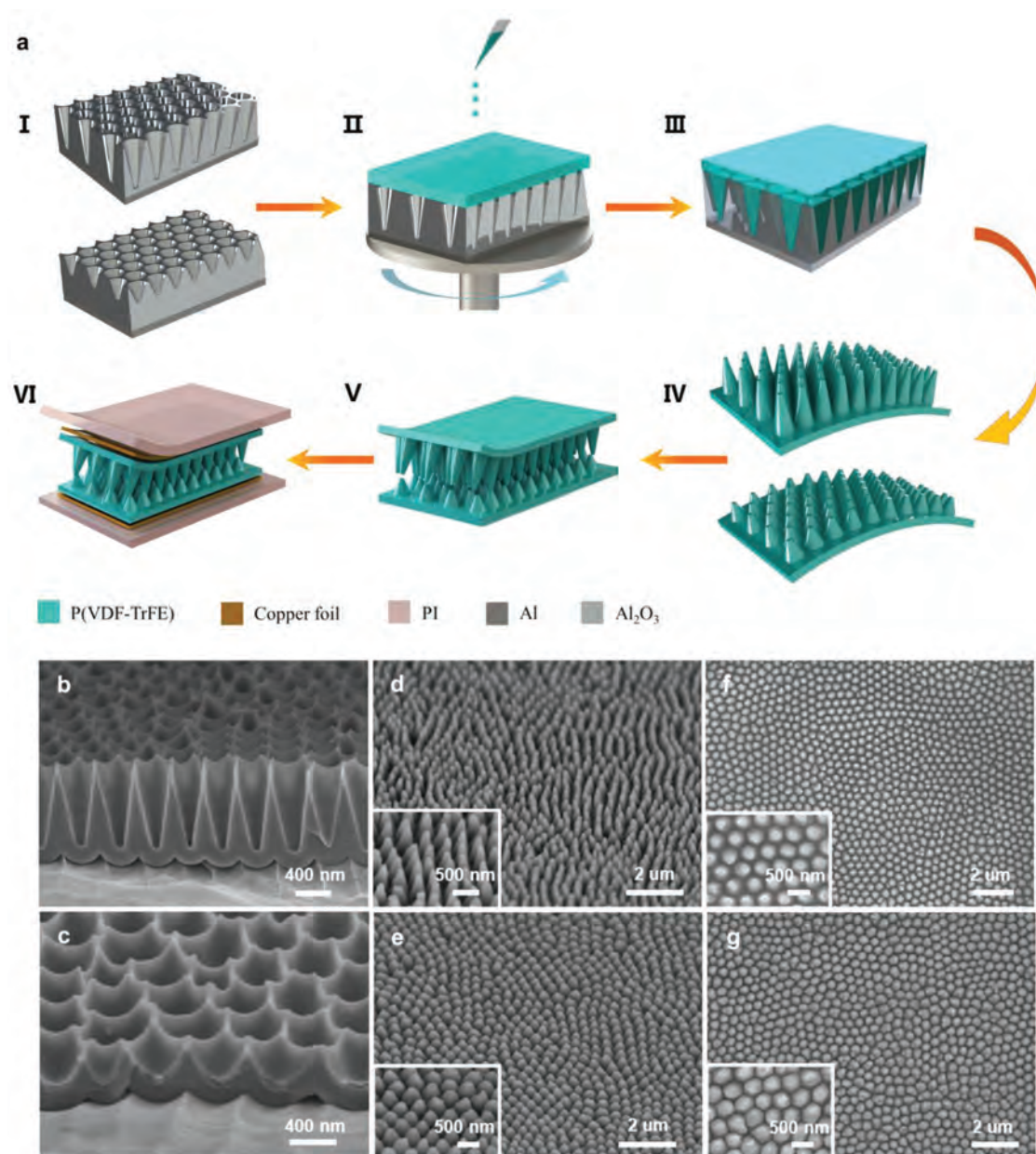


Figure 2. Preparation and characterization of capacitive tactile sensor. a) Flow chart illustrating the fabrication process for the interlocked nanocone arrays and corresponding schematic illustration of the assembled capacitive tactile sensor. The cross-sectional SEM images of cone-shaped nanoporous AAO templates with hole depth of b) 900 and c) 400 nm. The tilt-view SEM images of the two completed nanocone arrays with cone height of d) 900 and e) 400 nm. The top-view SEM images of the two completed nanocone arrays with cone height of f) 900 and g) 400 nm.

(Figure 2a-II). Followed by the solvent evaporation, and melt infiltration, the P(VDF-TrFE) is uniformly distributed in the AAO template, forming two nanocone arrays (Figure 2a-III). One should note that during the melt infiltration process, the heating temperature should be maintained between the melting (150 °C) and decomposition temperature (260 °C) of P(VDF-TrFE), so as to facilitate the complete infiltration of the polymer and avoid the destruction of molecular chain structure inside the polymer. The AAO templates are then removed via chemical etching process and two asymmetric P(VDF-TrFE) films with uniformly distributed nanocone arrays are subsequently attained (Figure 2a-IV). The two nanocone arrays are then arranged into interlocked configuration as depicted in Figure 2a-V. Finally, the proposed capacitive tactile sensor is assembled by laminating each nanocone array with Polyimide (PI) tape that is adhered by copper foil (Figure 2a-VI). The completed P(VDF-TrFE) film and the assembled sensor can be witnessed in Figure S1 (Supporting Information). With regard to the two AAO templates with hole depth of 900 and 400 nm, their cross-sectional scanning electron microscopy (SEM) images are respectively shown in Figure 2b,c. The tilt-view and top-view SEM images of the two completed nanocone arrays are also included in Figure 2d–g. From these images, it can be inferred that the AAO template is completely removed without residue on the surface and the nanocone arrays are well-arranged, successfully replicating the morphology of the AAO template. The surface morphologies of the fabricated nanocone arrays are further examined with the help of atomic force microscopy (AFM) and the results can be found in Figure S2 (Supporting Information), which shows that the surface morphologies of the nanocone arrays are consistent with that of the SEM images.

2.2. Sensing Performances and Mechanism Interpretation under Vertical Pressure

The sensing performance of the developed flexible capacitive tactile sensor is first evaluated by applying vertical pressure on it. In addition, extra two capacitive tactile sensors, of which the dielectric layers made of P(VDF-TrFE) are respectively nonpatterned (Plane–Plane configuration) and symmetric-nanocones (900–900 nm configuration), are manufactured to investigate the effect of the dielectric morphology on the sensing performance. The sensitivity (S) of a capacitive tactile sensor, which is a crucial factor for evaluating its performance, is usually defined as the tangent slope of the curve of the relative capacitance change with respect to the applied pressure,^[48,49] i.e.

$$S = \frac{\delta(\Delta C/C_0)}{\delta P} \quad (1)$$

where C_0 and ΔC are the initial capacitance and variation of capacitance, respectively, while P represents the imposed vertical pressure. For the three developed tactile sensors, Figure 3a summarizes their experimentally obtained relative capacitance changes under various vertical pressures. The results show that within the pressure range from 0 to 1000 Pa, the proposed

tactile sensor based on interlocked asymmetric-nanocones (900–400 nm configuration) features the best performance than the other two cases. In specific, when the imposed vertical pressure is below 100 Pa, the sensitivity of the proposed tactile sensor is $\approx 6.583 \text{ kPa}^{-1}$, which is a near 12-fold increase compared to that of the nonpatterned sensor. As the pressure is maintained within the range from 100 to 1000 Pa, the sensitivity is decreased to 0.125 kPa^{-1} . Similarly, the sensitivities of the sensor based on interlocked symmetric-nanocones are 3.527 and 0.113 kPa^{-1} , respectively, when the pressure is smaller and larger than 100 Pa. Nonetheless, for the tactile sensor based on nonpatterned dielectric layer, the sensitivity is 0.551 kPa^{-1} when the pressure is smaller than 100 Pa, and will be decreased to 0.103 kPa^{-1} with further increase of the pressure. Among the three tactile sensors, it is clear that the one based on interlocked asymmetric-nanocones exhibits the highest sensitivity. We further evaluate its responsiveness and repeatability by exerting/releasing five repetitive cycles of vertical pressure on it. Here, three vertical pressure values of 10, 100, and 1000 Pa are considered and successively applied on the tactile sensor. The real-time monitored results depicted in Figure 3b denote that the relative capacitance change rises as the loaded vertical pressure increases and the tactile sensor is able to maintain stable sensing performances in a broad pressure range. In addition, we investigate the response time of the proposed tactile sensor by placing an object on it (producing around 220 Pa pressure) and the relevant results are displayed in Figure 3c. The relative capacitance change drastically increases from the minimum to the maximum in $\Delta t_1 = 48 \text{ ms}$ (top-left inset) when the object is loaded on the developed tactile sensor. The corresponding recovery time when the object is unloaded from the sensor is found to be $\Delta t_2 = 36 \text{ ms}$ (top-right inset). These results indicate that the developed tactile sensor behaves similar to the human skin in terms of the response/recovery time (30–50 ms) and such performances are ascribed to the low viscoelasticity and special structure of the interlocked nanocones.^[27] In addition, the response/recovery time of extra typical pressures that is relatively evenly distributed within 1000 Pa are monitored in this work. Interestingly, all response/recovery time of the tactile sensor at the typical pressures not more than 1000 Pa are 48/36 ms, as shown in Figure S4 (Supporting Information). The results we obtained in this work are consistent with the conclusion stated by Yang and co-workers.^[50] The lightweight object detection of the tactile sensor is further investigated with the help of an object exhibiting a small pressure of $\approx 3 \text{ Pa}$. By loading the object atop the sensor, the relative capacitance change is steadily maintained in the vicinity of 2%, as shown in Figure 3d, implying the sensor is highly reliable to distinguish lightweight object. The response/recovery time of the tactile sensor at load/unload $\approx 3 \text{ Pa}$ vertical pressure is also 48/36 ms respectively, as shown in Figure S5 (Supporting Information). Moreover, as the long-term stability is quite important for practical applications, a pressure of $\approx 250 \text{ Pa}$ is repetitively loaded/unloaded on the tactile sensor to test its durability. As shown in Figure 3e, the profile of the relative capacitance change is considerably uniform and no obvious fatigue can be witnessed in 10 000 repetitive cycles. Table 1 lists recent published capacitive flexible tactile sensor to demonstrates the superiority of the proposed work as regards detection limit, sensitivity,

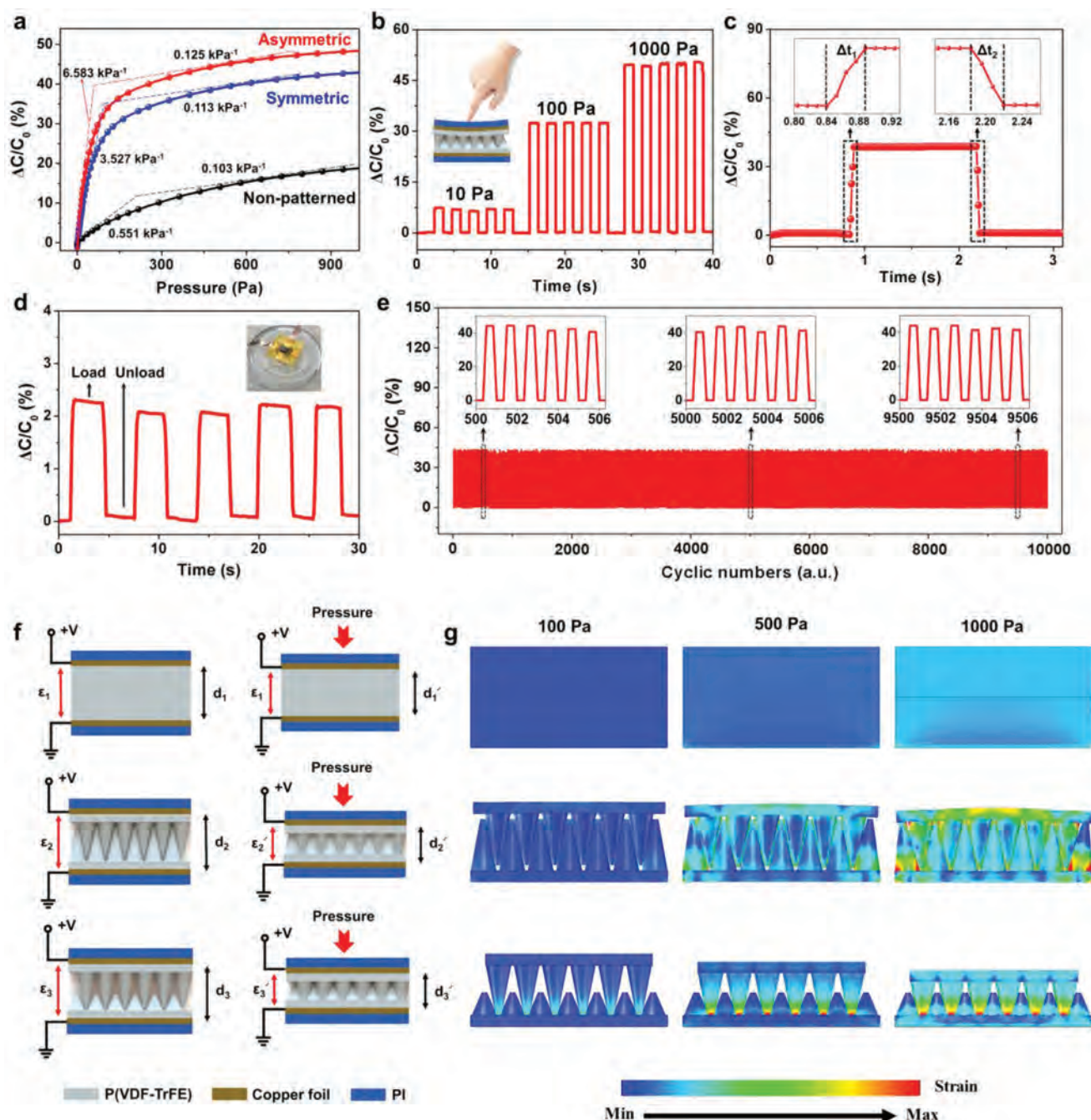


Figure 3. Sensing performances and sensing mechanisms of the capacitive tactile sensors under vertical pressure. a) Sensitivity curves of capacitive tactile sensors based on the interlocked asymmetric-nanocones (red), the interlocked symmetric-nanocones (blue) and the nonpatterned (black) dielectric layer. b) The tactile sensor repeated real-time response to vertical pressure of 10, 100, and 1000 Pa. c) Pressure response of the tactile sensor to a small pressure of ≈3 Pa. d) Real-time response of the tactile sensor to a small pressure of ≈220 Pa (the insets show response and recovery time). e) Stability of the tactile sensor tested for 10 000 cycles under a vertical pressure of ≈250 Pa (the insets show magnified signal under different time periods). f) Schematic illustration showing the structure deformation procedure when the dielectric layer is the nonpatterned, the symmetric-nanocones and the asymmetric-nanocones. g) FEA simulation showing the deformation and strain distribution of the nonpatterned, the symmetric-nanocones and the asymmetric-nanocones at vertical pressure of 100, 500, and 1000 Pa.

response/recovery time and stability in addition to the presented information on dielectric material, electrode material and dielectric layer structure.^[13,32,33,51–57]

The sensing mechanism of the three capacitive tactile sensors whose dielectric layer is constructed by nonpatterned, symmetric-nanocones, and asymmetric-nanocones,

respectively, is described in Figure 3f,g. For a capacitive tactile sensor, its capacitance (C) can be expressed as

$$C = \epsilon \frac{A}{4k\pi d} \quad (2)$$

where ϵ is the effective dielectric constant of the dielectric layer, k means electrostatic force constant, A represents the effective area of the two electrodes, and d stands for the separation distance between two electrodes. In principle, the variation in ϵ , A , and d could result in a change of the capacitance. Since the effective area of the electrode is almost invariant under different vertical pressure, the capacitance will be primarily determined by the ϵ and d . Figure 3f presents the schematic illustrations of the changes in ϵ and d when the same vertical pressure is applied to the aforementioned three sensors. It can be observed that the asymmetric-nanocones structured sensor is more likely to be compressed with rapidly decreased separation distance compared with nonpatterned and symmetric-nanocones types. In addition, following the general Lichtrecker mixing rule, the effective dielectric constant of the dielectric layer can be defined as

$$\epsilon^\alpha = V_{\text{air}}\epsilon_{\text{air}}^\alpha + V_{\text{P}}\epsilon_{\text{P}}^\alpha \quad (3)$$

where ϵ_{air} and ϵ_{P} are the dielectric constants of the air and P(VDF-TrFE), respectively, V_{air} and V_{P} are the volume fractions ($V_{\text{air}} + V_{\text{P}} = 1$) of air and P(VDF-TrFE), respectively, and α is the parameter determining the type of mixing rule.^[58,59] Given a high ϵ_{P} (around 8–10), low ϵ_{air} ($= 1$), and a large number of air gaps constituting the dielectric layer, the proposed structure easily makes the air squeeze out of the layer upon vertically applied pressure, leading to an enhanced ϵ^α . We further carried out FEA simulations to elaborate abovementioned analysis. For the dielectric layer with the three aforesaid configurations, their strain and stress distributions under various vertical pressures (100, 500, and 1000 Pa) are summarized in Figure 3g and Figure S3a (Supporting Information) respectively. Both figures reveal that the increased vertical pressure results in a strengthened strain and increased stress, and then we take

the 1000 Pa vertical pressure as an example to elaborate the effect of the dielectric layer configuration on the sensing performances. For the nonpatterned dielectric layer, the stress distribution is quite uniform on the planar interface and as a result no significant structure deformation or compression can be observed. However, for the dielectric layer involving interlocked symmetric-nanocones structure, a relatively high stress can be found on the cone interface contact between adjacent nanocones. Such effect leads to the phenomena that the air is squeezed out (increase in ϵ) and the dielectric layer is slightly compressed (decrease in d). In contrast to the previous two cases, the stress distribution in interlocked asymmetric-nanocones structure is highly strengthened and localized at a contact point as the apex of the upper nanocone can easily touch the base of the lower nanocone. As a result, the air gap and the dielectric nanocones can be greatly compressed than the other two cases. These simulation results imply that compared with the planar dielectric layer, the variation of ϵ and d can be greatly amplified in the interlocked nanocones and is more pronounced in the asymmetric-nanocones case, leading to a significantly enhanced sensitivity. From another perspective, the sensing mechanism based on the interlocked nanocones could also be explained by inspecting the deformation of the nanocones upon various vertical pressures (Figure S3b, Supporting Information). In the low-pressure range ($0-P_1$), a slightly increased pressure will cause the quick sliding of the nanocones and compression of the air gap, leading to the decreased d and increased ϵ . When a medium pressure (P_1-P_2) is applied to the sensor, the apex of the upper nanocone will touch the base surface of the lower nanocone. Considering the difficulty in compressing a polymer, this will hinder the quick variations of ϵ and d and in turn result in a relatively lower sensitivity. With further increasing of the pressure ($>P_2$), the sensitivity will be maintained at a very low level because the compression will be saturated and the variation of d is negligible. With the above analysis, we can conclude that the proposed capacitive tactile sensor based on interlocked asymmetric-nanocones can exhibit a high sensitivity at low pressure level, despite the fact that the sensitivity will degrade upon increased pressure.

Table 1. Performance comparison of recent published works based on flexible capacitive tactile sensor.

Dielectric material	Electrode material	Dielectric layer structure	Detection limit [Pa]	Sensitivity [kPa^{-1}]/Pressure range	Response/Recovery [ms]	Stability [cycle]	Ref.
Ecoflex	Ag	Planar	7.3	0.0224/<16 kPa	–	–	13
i-TPU	Ag	Pillar-shaped	1.8	2/<10 kPa	47/63	1200	32
PDMS	Au	Tilted micropillar	0.8	0.42/<1.5 kPa	<100	2000	33
Ecoflex	PEDOT:PSS	Planar (air gap)	–	0.0077/<10 kPa	–	1000	51
EIPH	ITO	Micropillars	–	2.33/<3 kPa	480/540	4000	52
VHB	Hydrogel	3D mesh	12	0.91/<2 kPa	–	–	53
OHGel	PAAm–NaCl	Wrinkled surface	–	2/<0.5 kPa	–	3000	54
PDMS/Si	PEDOT:PSS	Microspheres	2	1/<10 kPa	140/110	1000	55
PDMS	Ag NWs	Micro-array	7	2.04/<2 kPa	<100	3000	56
VHB	Hydrogel	Planar	–	0.09/<5 kPa	–	–	57
P(VDF-TrFE)	Cu	Interlocked nanocone	3	6.593/<100 Pa	48/36	10 000	This work

Meanwhile, we obviously note that the proposed interlocked asymmetric-nanocones structure also exhibits fast response time and excellent stability. The reasons for attaining these salient features are twofold: first, the viscoelasticity of the P(VDF-TrFE) will be significantly reduced when the nanocones are uniformly and densely distributed on it. As the nanocones can be evenly compressed upon to the applied pressure and will rapidly recover to the initial state when the pressure is eliminated, the response and recovery time can be very short. Second, the good stability of the interlocked nanocones can be attributed to the fact that the base of the nanocone is much larger than the apex, thus hindering the nanocones from collapse than conventional pillar structure.^[60,61] In a word, the interlocked asymmetric-nanocones can bring great benefits for a capacitive tactile sensor in terms of its sensitivity, response/recovery time, and stability.

2.3. Sensing Performances under Bending States

The performance of the proposed capacitive tactile sensor is further analyzed by placing it on the second joint of the index finger to investigate its sensing performance under various bending states. The finger is first maintained at a relaxed state with a bending angle of 0°, which is then turned into 10°, 30°, 50°, 70°, 90°, and 110° by bending the finger. The corresponding relative capacitance changes are measured to be ≈0%, ≈7%, ≈23%, ≈44%, ≈65%, ≈86%, and ≈105%, as shown in Figure 4a. Additionally, a near linear relationship can be found between the bending angle and the relative capacitance change, indicating that the proposed tactile sensor might be potentially utilized for monitoring the finger motion, as shown in Figure 4b.

We also investigate the sensing performance of the proposed sensor at the maximum bending angles of different finger joints. The tactile sensor is attached to the joints of the thumb, index finger, and middle finger whose maximum bending angles are 90°, 110°, and 120°, respectively, and the test for each case is repeated for five times. The relevant results depicted in Figure 4c imply that the proposed sensor can be used for the precise and stable detection of the bending angles by the readout of the capacitance value. Besides, the tactile sensor is adhered to the index finger and is subject to 500 times of cyclic bends under the bending angle of 60°. As can be witnessed in Figure 4d, the negligible signal drift within the 500 cyclic bends implies that the developed tactile sensor also exhibits excellent stability and durability. The inset photographs denoted as (1), (2), and (3) represent the process of grasping, releasing, and grasping of a plastic cup, corresponding to the bending, unfolding, and bending of the tactile sensor. Finally, we attach the developed tactile sensor on the joint of the index finger on a rubber glove so that it can be potentially used as a smart glove for detecting the bending motion of a finger. By gradually bending the finger, the capacitance is progressively increased and can be used to identify each bending state, as marked from “A” to “G” in Figure 4e. Similarly, the decrease of the capacitance value as marked from “G” to “M” represents the process of unfolding the finger. These results imply that the capacitive tactile sensor still offers high sensitivity, fast response/recovery time, and excellent stability in the bending states.

2.4. Applications in Vertical Mechanical Pressure

The capacitive tactile sensor to detect the vertical mechanical pressure in various applications is explored. The tactile sensor

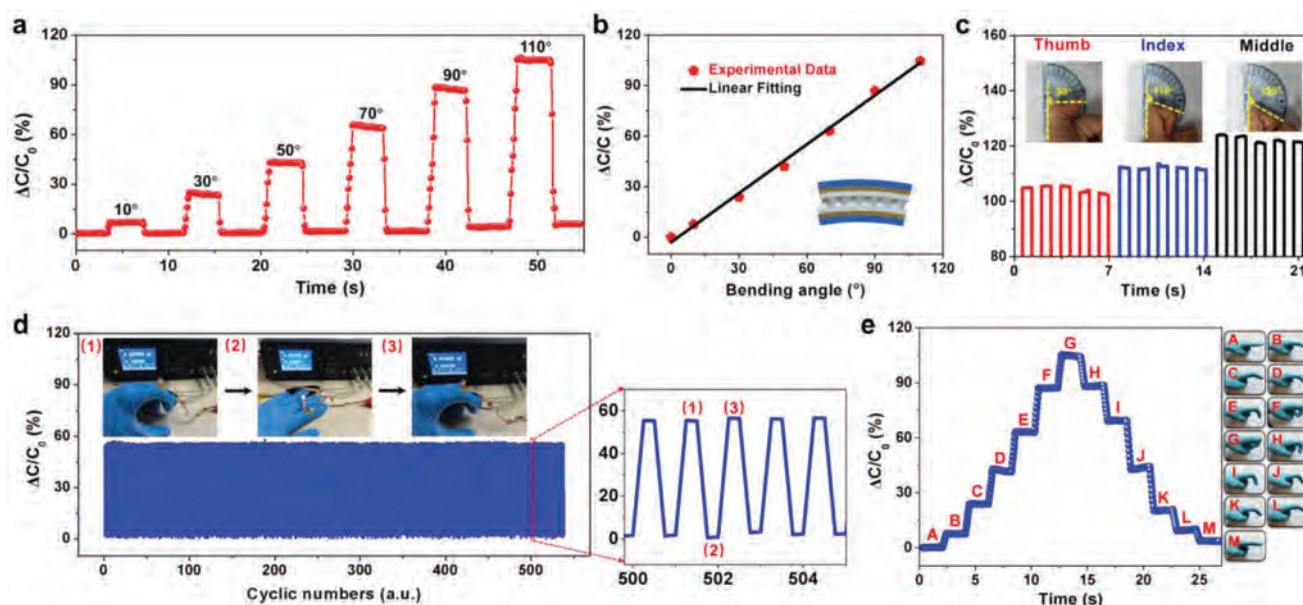


Figure 4. Sensing performances of the tactile sensor under bending states. a) The relative capacitance changes when bending the index finger at different angles (10°, 30°, 50°, 70°, 90°, and 110°). b) Relationship between relative capacitance changes and bending angle of the index finger joint. c) Capability to detect the maximum bending angle of the different finger (thumb, index, and middle). d) Bending responses over 500 cyclic tests (the inset is magnified cycle). e) The photographs when the finger is gradually bent (State A to G) and unfolded (State G to M). The corresponding relative capacitance changes from the gradual finger bending and unfolding over seven bending states.

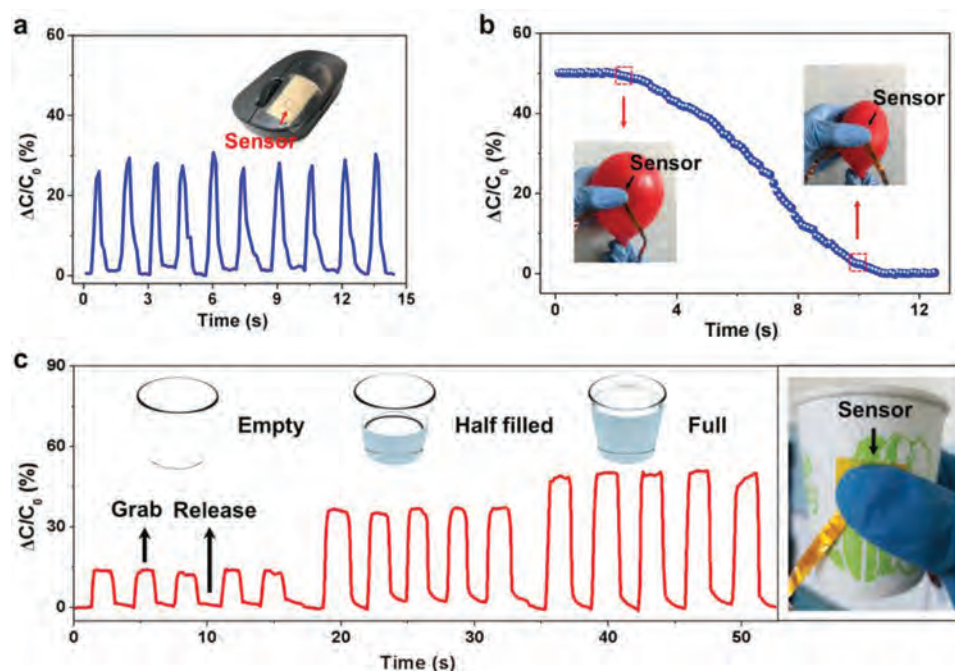


Figure 5. Application in vertical mechanical pressure. a) Relative capacitance changes of the tactile sensor when continuously press the left mouse button (the inset shows the tactile sensor attached to the left mouse button). b) Real-time pressure sensing of a flexible object by holding an inflating balloon with the human hand. c) Relative capacitance changes of the tactile sensor located between the paper cup and the thumb when grasping paper cups of different weights.

is first mounted on a left mouse button and undergoes a rhythmic pressing (≈ 160 Pa upon pressing, 10 cycles) by the fingertip. **Figure 5a** shows that the sensor can immediately respond to the pressing, attaining a synchronized and stable capacitance curve. Furthermore, the proposed tactile sensor is believed to be able to enable the real-time monitoring of vertical pressure on flexible objects. It is validated by grasping a balloon via a rubber glove, of which the fingertip is affixed with a tactile sensor. As shown in **Figure 5b**, a timely decrease in the relative capacitance change can be obtained when the pressure inside of the balloon is reduced via the deflation process. Finally, the sensor is attached to a paper cup so that it can feel the pressure upon grasping and releasing the cup. As shown in **Figure 5c**, grabbing and releasing an empty cup result in a relatively smaller change in the capacitance value. By filling the cup with water, it is evident that the capacitance value is significantly enlarged as the cup is getting heavier (half-filled to full). Besides, the relative capacitance change maintains quite stable in five cycles of grasping or releasing the cup. These results suggest that the proposed tactile sensor could be utilized to assist robots or human beings who have tactile sensation disorders to percept external feelings.

2.5. Applications in Human–Machine Interaction

The detection and recognition of sign language gestures are of great importance in wide applications such as communication with deaf-mutes, artificial intelligence, and human–machine interaction. To show the possibility of the proposed tactile sensor in recognizing sign language gestures, five identical

tactile sensors are implemented and respectively attached to each finger joint of a rubber glove to construct a “smart glove” as can be seen in **Figure 6a**. As each tactile sensor may undergo various bending angles upon to various gestures, their corresponding capacitance response also differs and thus a real-time recognition of sign language gestures could be achieved. For instance, the relative capacitance changes affiliated with the five unfolded fingers will be maintained at very low level. By individually showing the sign language gesture of letter “A,” “B,” “C,” “D,” “E,” and “F,” the relative capacitance change relating to each finger can reach different values, as can be seen in **Figure 6b**. Furthermore, the continuous varying sign language gestures representing the sentence “I LOVE Y” have been synchronously recognized by the “smart glove” via viewing the rapidly varied capacitance values. All in all, similar and complex gestures can be recognized or differentiated by the proposed tactile sensors considering its salient features including the fast and high response sensitivity at different bending angles.

The applicability of an individual tactile sensor is inevitably limited as it can only provide the pressure information at one local point. The perception of the spatial distribution of pressures could be realized by integrating multiple tactile sensors that form a sensor array. As depicted in **Figure 6c**, a sensor array occupying a footprint of $10\text{ mm} \times 10\text{ mm}$ is constructed by incorporating 5×5 pixels of the tactile sensors, with each tactile sensor featuring a size of $1\text{ mm} \times 1\text{ mm}$. Details of the procedure to construct the array can be found in the experimental section. Three plastic objects in the shapes of “U,” “J,” and “N” with corresponding weights of 0.644, 0.641, and 0.652 g, are subsequently used to test the spatial distinguishable ability of the sensor array. As depicted in **Figure 6d**, the 3D histograms

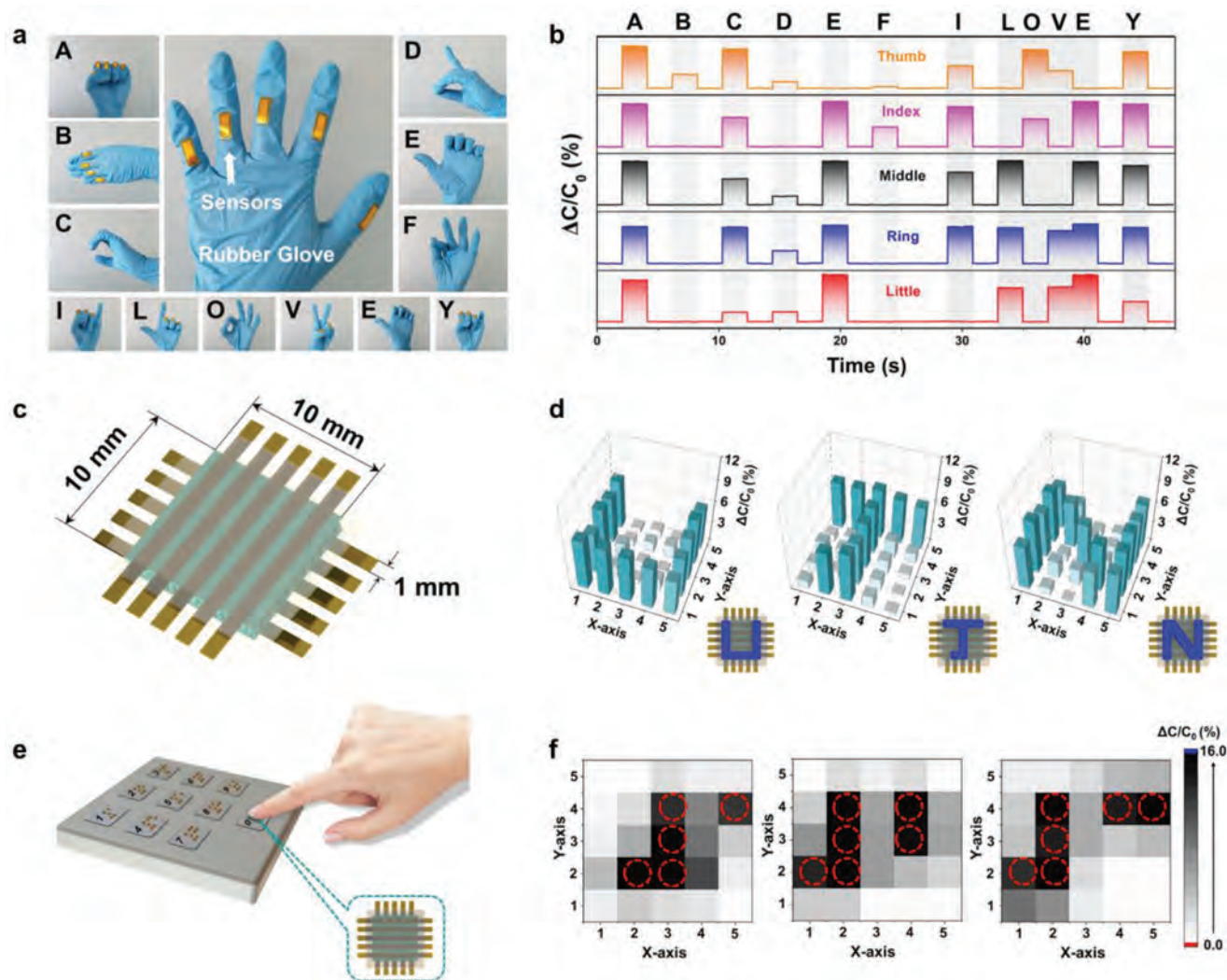


Figure 6. Application in human-machine interaction. a) Photograph of a glove with five tactile sensors attached on its joints, and images of twelve different sign language gestures. b) Real-time monitored relative capacitance changes under various sign language gestures as shown in (a). c) Schematic illustration of the tactile sensor based on a 5 × 5 pixel array. d) Spatial pressure distribution capability test of the 5 × 5 sensor arrays using plastic boards that are shaped like the letters “U,” “J,” and “N,” which correspond to the letters of the insets. e) The image of a numeric keypad with Braille. f) The relative capacitance changes of the three Braille numbers of “1,” “2,” and “3.”

reveal that high relative capacitance changes affiliated with the sensor array can only be obtained at the location where the objects are on-site. The results indicate that the proposed tactile sensors can be assembled to an array with a spatial-pressure differentiation ability comparable to the human skin and thus can be potentially used in the applications such as wearable electronic device and flexible robot.

Blind people usually receive the information by touching a group of raised dots that are printed on a platform or so-called Braille. We show that the constructed tactile sensor array can be also used as an artificial fingertip to read the Braille. Figure 6e shows the schematic illustration of a Braille numeric keypad, in which each Braille (a single raised dot) is smaller than 1 mm × 1 mm and therefore can be completely covered by the artificial fingertip (10 mm × 10 mm). It can be understood that as the artificial fingertip touches the Braille, the tactile sensors are anticipated to undergo various structural deformations,

leading to distinct capacitance changes that can be used to decode the Braille. Plotted in Figure 6f are the relative capacitance changes of the three Braille numbers of “1,” “2,” and “3” measured by the proposed artificial fingertip. The high relative capacitance changes are only found at the position where a raised dot is located (indicated by a mark in red dashed circle). The result suggests that the proposed artificial fingertip can have promising prospects in assisting the Braille recognition or the auxiliary of disabled.

2.6. Applications in Recognition of Physiological Signals

In light of its high sensitivity and excellent mechanical stability with respect to the applied pressure, the proposed tactile sensor can be used to monitor the tiny pressures stemming from human physiological activities such as the pulse beating, eye

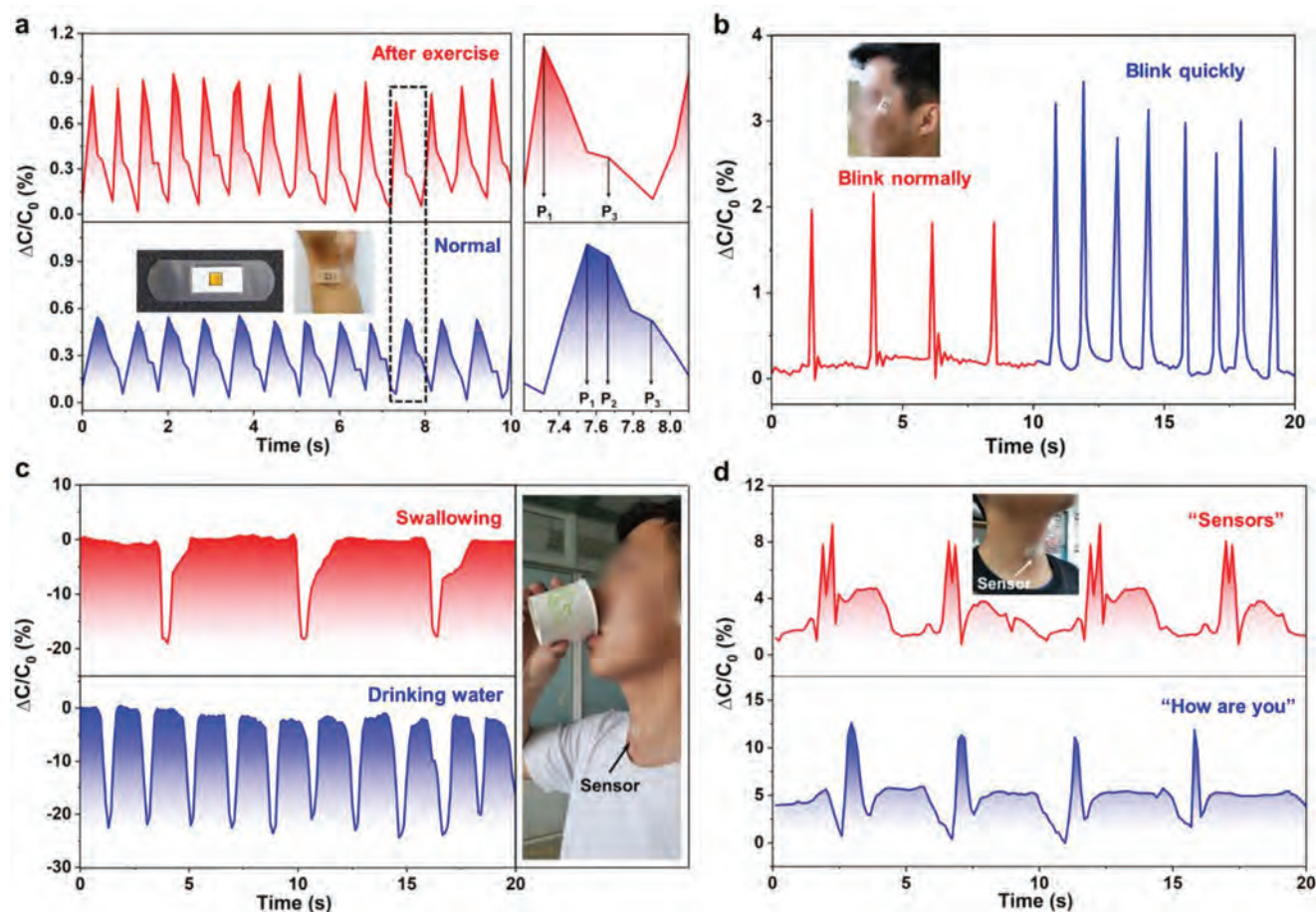


Figure 7. Application in recognition of physiological signals. a) Relative capacitance changes of the wrist pulse before and after exercise (the inset shows magnified view of single pulse). b) Real-time relative capacitance changes for corresponding eye blinking normally and quickly. c) Monitoring different movements of throat such as swallowing and drinking water. d) Response curves of the tactile sensor for monitoring tiny muscle movement and vibrations during speech.

blink, and swallow. The pulse is known as an important physiological signal that is induced by the heart muscle contracting and pumping blood from the chambers into the arteries and thus can be used to evaluate the physical or mental state of a human being. For instance, some information relating to the cardiovascular disease can be acquired by monitoring the pulse waveform, of which the shape is closely related to the disease. We first carry out a simple test by mounting a tactile sensor on the wrist for real-time monitoring the pulse waveform before and after exercise. As shown in **Figure 7a**, the pulse frequencies before and after exercise is 72 and 84 beats per minute, respectively. Besides, the amplitudes in the two pulse waveforms also differ a lot. The magnified inset shows one of the pulse periods before and after exercise, from which one could observe the percussion wave (P_1), tidal wave (P_2), and diastolic wave (P_3) that are respectively related to the systolic/diastolic blood pressure, ventricular pressure, and heart rate. As compared with the case before exercise, the pulse waveform presents quite different features including the enhanced P_1 and vanished P_2 after exercise, which might be attributed to the change of the heart or ventricular pump. The above-mentioned results on pulse frequencies, pulse amplitudes and wave shape are in good agreement with human's understanding of pulse, indicating that the

proposed sensor is totally feasible to detect pulse signal. Sudden eye blinking is thought to be a stress-induced self-sobering behavior that occurs when people feel tired, sleepy, or get facial nerve diseases such as Parkinsonism and facial spasm. We further fix the tactile sensor at the eye corner to monitor the eye blinking. It can be anticipated that the compressive stress that is induced during the eye closing will enable the tactile sensor to have much higher relative capacitance change than that in the process during eye opening, making it possible to detect the opening and closing of the eye. **Figure 7b** shows the response of the tactile sensor when the eye blinking is conducted at a normal or fast speed, and it is obvious that the two states can be effectively distinguished in frequency. Meanwhile, two kinds of magnitude of capacitance can also be detected due to employing greater force in the rapid blink. In addition, the tactile sensor is attached to the throat to monitor the motions and vibrations of the trachea and esophagus so that it can be possibly used to the real-time speech recognition or even the prevention of throat diseases. **Figure 7c** shows the real-time monitored relative capacitance changes during swallowing saliva and drinking water. As the two processes are accompanied with different degrees of throat muscle motions (due to the existence of water), the tactile sensor suffers dissimilar shrinkage deformations which

in turn result in two various relative capacitance responses. With the purpose of showing its potential application in speech recognition, the same tactile sensor is further tested upon speech. As plotted in Figure 7d, the capacitance responses are recorded when the word “Sensors” or the sentence “How are you” are repeatedly pronounced for four times. It can be clearly seen that the two response curves exhibit different features, while in each curve the four pronunciation-induced responses are quite similar, implying that the proposed tactile sensor has the ability of stably distinguish various pronunciations. These results demonstrate that the proposed tactile sensor might be utilized for pre-diagnosing the disease such as cough by real-time monitoring the amplitude and frequency characteristics of the capacitance response curve. In short, the proposed tactile sensor shows excellent performances in real-time monitoring the human physiological signals under the condition of good conform nature to the skin and could be used in preventing or diagnosing a wide range of diseases such as the cardiovascular and cerebrovascular diseases, neurological diseases, and cardiopulmonary diseases.

3. Conclusion

In conclusion, inspired by the interlocked microridges structures between dermis and epidermis in human skin, we developed a facile method, combining a simple melt infiltration process of P(VDF-TrFE) and a commercial cone-shaped nanoporous AAO transfer method to fabricate a highly morphology-controllable and highly sensitive capacitive tactile sensor. Based on FEA simulations and experimental results, the uniformly and densely distributed interlocked nanocones were shown to be capable of highly concentrating the stress, leading to high performances of the proposed tactile sensor, including an ultrahigh sensitivity, an ultralow detection limit, a fast response/recovery time and excellent stability. In addition, we also examined the proposed sensor sensing performances under bending states, which revealed that the relative capacitance change was almost linearly proportional to the bending angle, enabling the monitoring of the bending motion in various applications. More importantly, the proposed sensor/sensor arrays were applied in several practical applications, which successfully verified the high sensing performance of the proposed sensor. We fully believe that the combination of the interlocked nanocone structure and the sensing material of P(VDF-TrFE), along with the AAO template-assisted fabrication method for implementing the proposed capacitive tactile sensor, will be of great significance for the development of flexible electronic technology on human-machine interaction, physiological signal monitoring, biomedical prosthetics as well as disease prevention and diagnosis.

4. Experimental Section

Fabrication of P(VDF-TrFE) Nanocone Arrays: 5 wt% of P(VDF-TrFE) solution was prepared by dissolving P(VDF-TrFE) powder (Kunshan Hisense Electronics Co., Ltd, China) with a composition of 70:30 in DMF, and then the solution was sonicated until the P(VDF-TrFE) powder was completely dissolved. A few drops of the P(VDF-TrFE)/DMF solutions were dripped using a pipette onto cone-shaped

nanoporous AAO templates (bottom diameter of 450 nm, top diameter of 100 nm, pore depth of 900 nm/400 nm, Shenzhen Topmembranes Technology Co., Ltd, China), and then spin-coated at 1000 rpm for 600 s. Additionally, the template was ultrasonically cleaned for 30 min in a mixed solution of acetone, 2-propanol and deionized water (1:1:1 by volume ratios) before dropping. Subsequently, the P(VDF-TrFE)/AAO was left for 24 h on a hot plate at 30 °C to remove the DMF solvent. Following the evaporation of the solvent, the P(VDF-TrFE)/AAO was placed in the muffle furnace and maintained at a temperature of 180 °C for 1 h, which was higher than the melting point of P(VDF-TrFE), resulting in the infiltration of melting P(VDF-TrFE) into cone-shaped nanoporous AAO templates and the formation of nanocones within the cone-shaped nanoporous, and then the sample was slowly cooled to room temperature to cure the nanocone arrays. The freestanding P(VDF-TrFE) nanocone array was obtained after dissolving the cone-shaped nanoporous AAO template. The back of aluminum oxide layer was first removed by immersing the P(VDF-TrFE)/AAO in 4 M NaOH solution for 30 min. After that, by dissolving the P(VDF-TrFE)/AAO in a mixture of 2 M CuCl₂ solution in water and 36 wt% HCl solution in water (CuCl₂ solution: HCl solution: H₂O 2:1:2 in volume) for 10 min, the Al layer can be dissolved. Finally, the P(VDF-TrFE)/AAO was immersed in 4 M NaOH solution for 2 h, the remaining aluminum oxide layer can be removed and P(VDF-TrFE) nanocone array was obtained. It should be noted that the fabricated P(VDF-TrFE) nanocone array is not subjected to the high voltage treatment to polarize it in this work, so that the P(VDF-TrFE) piezoelectric effect can be ignored.

Assembly of the Flexible Capacitance Tactile Sensor: Two different P(VDF-TrFE) nanocone films with patterned surfaces facing each other were arranged into interlocked configuration. Subsequently, two pieces of the copper foil were attached to the side of the PI tape with adhesive layer as electrodes. Finally, PI tape with copper electrode was attached to the top and bottom sides of interlocked nanocone film for packaging, and the remaining copper foil can be used as lead wire to form a capacitive tactile sensor.

Fabrication of the Pixel Array: Attach five pieces of copper foil (1 mm × 20 mm) based on 1 mm intervals to the PI tape as a strip electrode array, and another strip electrode array was made in the same way. Then the two strip electrode arrays were cross combined with the interlocked nanocone film to form 25 cross-link areas (1 mm × 1 mm for each area), thus assembling a facile 5 × 5 capacitive tactile sensor pixel array.

Structural Characterization and Electrical Measurement: Field emission scanning electron microscopy (FESEM) images were obtained on a Regulus-8100. Atomic force microscopy images were measured using Dimension Icon. Tactile sensor capacitance measurements were recorded on an Agilent (E4980AL) Precision LCR meter.

Supporting Information

Supporting Information is available from the Wiley Online Library or from the author.

Acknowledgements

This work was supported by the National Natural Science Foundation of China under Grant (61604060 and 61805101), Shandong Provincial Natural Science Foundation of China under Grant (ZR2017JL027 and ZR2019BF013) and China Postdoctoral Science Foundation under Grant (2018M632605). The volunteers (Hongliang Li and Hongsen Niu) agreed to all tests with informed consent, including the eye corner, and throat experimental study and biocompatibility tests.

Conflict of Interest

The authors declare no conflict of interest.

Keywords

anodized aluminum oxide, capacitive tactile sensors, electronic skin, highly morphology-controllable, interlocked asymmetric-nanocone arrays, P(VDF-TrFE)

Received: August 24, 2019
Revised: November 15, 2019
Published online:

- [1] J. Gould, *Nature* **2018**, 563, S84.
- [2] P. Delmas, J. Hao, L. Rodat-Despoix, *Nat. Rev. Neurosci.* **2011**, 12, 139.
- [3] C. Wang, K. Xia, H. Wang, X. Liang, Z. Yin, Y. Zhang, *Adv. Mater.* **2019**, 31, 1801072.
- [4] W. A. D. M. Jayathilaka, K. Qi, Y. Qin, A. Chinnappan, W. Serrano-Garcia, C. Baskar, H. Wang, J. He, S. Cui, S. W. Thomas, S. Ramakrishna, *Adv. Mater.* **2019**, 31, 1805921.
- [5] T. Q. Trung, N.-E. Lee, *Adv. Mater.* **2016**, 28, 4338.
- [6] C.-B. Huang, S. Witomska, A. Aliprandi, M.-A. Stoeckel, M. Bonini, A. Ciesielski, P. Samori, *Adv. Mater.* **2019**, 31, 1804600.
- [7] G. Schwartz, B. C.-K. Tee, J. Mei, A. L. Appleton, D. H. Kim, H. Wang, Z. Bao, *Nat. Commun.* **2013**, 4, 1859.
- [8] M. Zhu, Q. Shi, T. He, Z. Yi, Y. Ma, B. Yang, T. Chen, C. Lee, *ACS Nano* **2019**, 13, 1940.
- [9] C. Wang, X. Li, E. Gao, M. Jian, K. Xia, Q. Wang, Z. Xu, T. Ren, Y. Zhang, *Adv. Mater.* **2016**, 28, 6640.
- [10] M. Liao, P. Wan, J. Wen, M. Gong, X. Wu, Y. Wang, R. Shi, L. Zhang, *Adv. Funct. Mater.* **2017**, 27, 1703852.
- [11] D. J. Lipomi, M. Vosgueritchian, B. C.-K. Tee, S. L. Hellstrom, J. A. Lee, C. H. Fox, Z. Bao, *Nat. Nanotechnol.* **2011**, 6, 788.
- [12] Z. Zhu, R. Li, T. Pan, *Adv. Mater.* **2018**, 30, 1705122.
- [13] Q. Hua, J. Sun, H. Liu, R. Bao, R. Yu, J. Zhai, C. Pan, Z. L. Wang, *Nat. Commun.* **2018**, 9, 244.
- [14] D. Y. Park, D. J. Joe, D. H. Kim, H. Park, J. H. Han, C. K. Jeong, H. Park, J. G. Park, B. Joung, K. J. Lee, *Adv. Mater.* **2017**, 29, 1702308.
- [15] J. Zhong, Y. Ma, Y. Song, Q. Zhong, Y. Chu, I. Karakurt, D. B. Bogy, L. Lin, *ACS Nano* **2019**, 13, 7107.
- [16] Z. Chen, Z. Wang, X. Li, Y. Lin, N. Luo, M. Long, N. Zhao, J.-B. Xu, *ACS Nano* **2017**, 11, 4507.
- [17] Q.-J. Sun, X.-H. Zhao, Y. Zhou, C.-C. Yeung, W. Wu, S. Venkatesh, Z.-X. Xu, J. J. Wylie, W.-J. Li, V. A. L. Roy, *Adv. Funct. Mater.* **2019**, 29, 1808829.
- [18] L.-Q. Tao, K.-N. Zhang, H. Tian, Y. Liu, D.-Y. Wang, Y.-Q. Chen, Y. Yang, T.-L. Ren, *ACS Nano* **2017**, 11, 8790.
- [19] Y. Pang, K. Zhang, Z. Yang, S. Jiang, Z. Ju, Y. Li, X. Wang, D. Wang, M. Jian, Y. Zhang, R. Liang, H. Tian, Y. Yang, T.-L. Ren, *ACS Nano* **2018**, 12, 2346.
- [20] M. Ha, S. Lim, S. Cho, Y. Lee, S. Na, C. Baig, H. Ko, *ACS Nano* **2018**, 12, 3964.
- [21] K. Dong, Z. Wu, J. Deng, A. C. Wang, H. Zou, C. Chen, D. Hu, B. Gu, B. Sun, Z. L. Wang, *Adv. Mater.* **2018**, 30, 1804944.
- [22] M. Xu, T. Zhao, C. Wang, S. L. Zhang, Z. Li, X. Pan, Z. L. Wang, *ACS Nano* **2019**, 13, 1932.
- [23] J. Chang, K. B. Toga, J. D. Paulsen, N. Menon, T. P. Russell, *Macromolecules* **2018**, 51, 6764.
- [24] Y. Joo, J. Byun, N. Seong, J. Ha, H. Kim, S. Kim, T. Kim, H. Im, D. Kim, Y. Hong, *Nanoscale* **2015**, 7, 6208.
- [25] A. Singh, S. Das, M. Bharathkumar, D. Revanth, A. R. B. Karthik, B. S. Sastry, V. R. Rao, *Mater. Res. Express* **2016**, 3, 075702.
- [26] S. Pyo, J. Choi, J. Kim, *Adv. Electron. Mater.* **2018**, 4, 1700427.
- [27] B. C.-K. Tee, A. Chortos, R. R. Dunn, G. Schwartz, E. Eason, Z. Bao, *Adv. Funct. Mater.* **2014**, 24, 5427.
- [28] X. Shuai, P. Zhu, W. Zeng, Y. Hu, X. Liang, Y. Zhang, R. Sun, C.-P. Wong, *ACS Appl. Mater. Interfaces* **2017**, 9, 26314.
- [29] S. Chen, S. Peng, W. Sun, G. Gu, Q. Zhang, X. Guo, *Adv. Mater. Technol.* **2019**, 4, 1800681.
- [30] H. Jang, H. Yoon, Y. Ko, J. Choi, S.-S. Lee, I. Jeon, J.-H. Kim, H. Kim, *Nanoscale* **2016**, 8, 5667.
- [31] S. C. B. Mannsfeld, B. C.-K. Tee, R. M. Stoltenberg, C. V. H.-H. Chen, S. Barman, B. V. O. Muir, A. N. Sokolov, C. Reese, Z. Bao, *Nat. Mater.* **2010**, 9, 859.
- [32] M. L. Jin, S. Park, Y. Lee, J. H. Lee, J. Chung, J. S. Kim, J.-S. Kim, S. Y. Kim, E. Jee, D. W. Kim, J. W. Chung, S. G. Lee, D. Choi, H.-T. Jung, D. H. Kim, *Adv. Mater.* **2017**, 29, 1605973.
- [33] Y. Luo, J. Shao, S. Chen, X. Chen, H. Tian, X. Li, L. Wang, D. Wang, B. Lu, *ACS Appl. Mater. Interfaces* **2019**, 11, 17796.
- [34] S. Park, H. Kim, M. Vosgueritchian, S. Cheon, H. Kim, J. H. Koo, T. R. Kim, S. Lee, G. Schwartz, H. Chang, Z. Bao, *Adv. Mater.* **2014**, 26, 7324.
- [35] J. Park, Y. Lee, M. H. Barbee, S. Cho, S. Cho, R. Shanker, J. Kim, J. Myoung, M. P. Kim, C. Baig, S. L. Craig, H. Ko, *Adv. Mater.* **2019**, 31, 1808148.
- [36] Y. Cao, T. Li, Y. Gu, H. Luo, S. Wang, T. Zhang, *Small* **2018**, 14, 1703902.
- [37] J. Park, Y. Lee, J. Hong, M. Ha, Y.-D. Jung, H. Lim, S. Y. Kim, H. Ko, *ACS Nano* **2014**, 8, 4689.
- [38] J. Shi, L. Wang, Z. Dai, L. Zhao, M. Du, H. Li, Y. Fang, *Small* **2018**, 14, 1800819.
- [39] J. Park, Y. Lee, J. Hong, Y. Lee, M. Ha, Y. Jung, H. Lim, S. Y. Kim, H. Ko, *ACS Nano* **2014**, 8, 12020.
- [40] Y. Lee, J. Park, S. Cho, Y.-E. Shin, H. Lee, J. Kim, J. Myoung, S. Cho, S. Kang, C. Baig, H. Ko, *ACS Nano* **2018**, 12, 4045.
- [41] J. Park, M. Kim, Y. Lee, H. S. Lee, H. Ko, *Sci. Adv.* **2015**, 1, e1500661.
- [42] B. Su, S. Gong, Z. Ma, L. W. Yap, W. Cheng, *Small* **2015**, 11, 1886.
- [43] Z. Qiu, Y. Wan, W. Zhou, J. Yang, J. Yang, J. Huang, J. Zhang, Q. Liu, S. Huang, N. Bai, Z. Wu, W. Hong, H. Wang, C. F. Guo, *Adv. Funct. Mater.* **2018**, 28, 1802343.
- [44] P. Nie, R. Wang, X. Xu, Y. Cheng, X. Wang, L. Shi, J. Sun, *ACS Appl. Mater. Interfaces* **2017**, 9, 14911.
- [45] Y. Wan, Z. Qiu, Y. Hong, Y. Wang, J. Zhang, Q. Liu, Z. Wu, C. F. Guo, *Adv. Electron. Mater.* **2018**, 4, 1700586.
- [46] T. Li, H. Luo, L. Qin, X. Wang, Z. Xiong, H. Ding, Y. Gu, Z. Liu, T. Zhang, *Small* **2016**, 12, 5042.
- [47] R. Brito-Pereira, C. Ribeiro, S. Lanceros-Mendez, P. Martins, *Composites, Part B* **2017**, 120, 97.
- [48] Y. Wan, Z. Qiu, J. Huang, J. Yang, Q. Wang, P. Lu, J. Yang, J. Zhang, S. Huang, Z. Wu, C. F. Guo, *Small* **2018**, 14, 1801657.
- [49] Y. Wan, Y. Wang, C. F. Guo, *Mater. Today Phys.* **2017**, 1, 61.
- [50] J. Yang, S. Luo, X. Zhou, J. Li, J. Fu, W. Yang, D. Wei, *ACS Appl. Mater. Interfaces* **2019**, 11, 14997.
- [51] H. Shi, M. Al-Rubaia, C. M. Holbrook, J. Miao, T. Pinto, C. Wang, X. Tan, *Adv. Funct. Mater.* **2019**, 29, 1809116.
- [52] M.-J. Yin, Z. Yin, Y. Zhang, Q. Zheng, A. P. Zhang, *Nano Energy* **2019**, 58, 96.
- [53] X.-Y. Yin, Y. Zhang, X. Cai, Q. Guo, J. Yang, Z. L. Wang, *Mater. Horiz.* **2019**, 6, 767.
- [54] W. Xie, J. Duan, H. Wang, J. Li, R. Liu, B. Yu, S. Liu, J. Zhou, *J. Mater. Chem. A* **2018**, 6, 24114.
- [55] H. Kim, G. Kim, T. Kim, S. Lee, D. Kang, M.-S. Hwang, Y. Chae, S. Kang, H. Lee, H.-G. Park, W. Shim, *Small* **2018**, 14, 1703432.
- [56] L. Ma, X. Shuai, Y. Hu, X. Liang, P. Zhu, R. Sun, C.-P. Wong, *J. Mater. Chem. C* **2018**, 6, 13232.
- [57] Z. Lei, P. Wu, *ACS Nano* **2018**, 12, 12860.
- [58] Y. Wu, X. Zhao, F. Li, Z. Fan, *J. Electroceram.* **2003**, 11, 227.
- [59] K. Lichtenecker, *Phys. Z.* **1926**, 27, 115.
- [60] Y. Cho, G. Kim, Y. Cho, S. Y. Lee, H. Minsky, K. T. Turner, D. S. Gianola, S. Yang, *Adv. Mater.* **2015**, 27, 7788.
- [61] Y. Zhang, C.-W. Lo, J. A. Taylor, S. Yang, *Langmuir* **2006**, 22, 8595.